International Journal of Remote Sensing
Vol. 27, No. 11, June 2006, 2303–2321

Taylor & Francis
Taylor & Francis Group

Monitoring the maximum turbidity zone and detecting fine-scale turbidity features in the Gironde estuary using high spatial resolution satellite sensor (SPOT HRV, Landsat ETM+) data

D. DOXARAN*†, P. CASTAING‡ and S. J. LAVENDER†

†University of Plymouth, School of Earth, Ocean and Environmental Sciences, Drake Circus, Plymouth PL4 8AA, UK

‡Université Bordeaux I, Département de Géologie et Océanographie, UMR 5805 EPOC, Avenue des Facultés, 33405 Talence cedex, France

This study concerns the quantification of suspended particulate matter in the highly turbid estuarine waters of the Gironde, France, from high spatial resolution remotely sensed data, SPOT (Satellite Pour l'Observation de la Terre) High Resolution Visible (HRV), Landsat Enhanced Thematic Mapper Plus (ETM+). The methodology is based on calibration relationships established between the remote sensing reflectance (R_{rs}) signal and suspended particulate matter concentration (*SPM*), from *in situ* optical measurements. These relationships are valid in the long term as R_{rs} ratios between near-infrared (NIR) and visible wavebands are relatively independent of the particle grain-size and mineralogy. Consequently, they can be applied to satellite images, even if no simultaneous *in situ* measurements are carried out concurrently with the satellite overpass.

Selected satellite sensor data are corrected for atmospheric effects using radiative transfer code, then converted into surface water *SPM* concentrations according to the established calibration relationships. Resulting *SPM* maps are presented for different river flow and tidal conditions. These maps are used to locate the maximum turbidity zone and observe its tidal and seasonal movements. The high spatial resolution of SPOT HRV and Landsat ETM+ satellite sensor data also shows detailed turbidity features in the estuary, resulting from re-suspension phenomena over banks and turbulent currents.

Keywords: Estuary; Sediment; Turbidity; SPOT HRV, Landsat ETM+, Gironde

1. Introduction

Spatial remote sensing can be an efficient tool for mapping terrigeneous substances in coastal waters, and hence provide monitoring agencies with water quality maps. Recent work in highly turbid estuarine waters has shown that algorithms can be developed to quantify suspended matter concentrations (*SPM*) using reflectance ratios. The relationships between reflectance ratios and *SPM* are relatively insensitive to the particle characteristics (Moore *et al.* 1999, Doxaran *et al.* 2002a) and illumination conditions (e.g. cloud cover) (Doxaran *et al.* 2003). As a

*Corresponding author. Email: ddoxaran@plymouth.ac.uk

International Journal of Remote Sensing
ISSN 0143-1161 print/ISSN 1366-5901 online
http://www.tandf.co.uk/journals
DOI: 10.1080/01431160500396865

consequence, a single relationship has been obtained in the Gironde estuary (south-west France) from measurements carried out during a six-year period (1996–2001) (Doxaran *et al.* 2003). It can be used to estimate *SPM* from satellite data recorded during this period, even if simultaneous field measurements are absent.

In coastal waters, estuaries are complex environments where dissolved and particulate matter, drained by rivers in upland basins, are mixed with marine water and substances. As a consequence of the tidal asymmetry and residual density circulation, a maximum turbidity zone (MTZ) is generally formed in macrotidal estuaries where most of the suspended particles are trapped (e.g. Allen *et al.* 1977). Depending on the upland basins, these particles are mainly cohesive sediments (clays and silts), which settle and can form fluid mud layers during neap tides. The presence of a MTZ strongly affects biological processes by influencing the turbidity and hence water column light penetration, which is a factor in controlling primary production. The understanding of fine sediment transport, notably in the high-turbidity zone, is also necessary to predict the fate of eventual pollutants and to design dredging strategies. Regular and spatially adapted observations are needed for the initialization and validation of numerical hydro-sedimentary models (Siegel *et al.* 1999, Douillet *et al.* 2001), in order to quantify sedimentary fluxes and estimate the fluvial solid discharges to the ocean.

The objective of this study was to highlight the information that can be extracted from satellite data in terms of sediment transport dynamics in estuaries. The selected study area is the Gironde estuary (figure 1). It is macrotidal and presents a well-developed MTZ. Numerous studies of sediment transport have been performed in this area (e.g. Allen *et al.* 1977, Castaing 1981, Cancino and Neves 1999, Le Hir *et al.* 2001, Sottolichio *et al.* 2001). The method developed by Doxaran *et al.* (2002a, b, 2003), based on a simple atmospheric correction scheme and semi-empirical quantification algorithm, was applied to a set of satellite images recorded from 1996 to 2001. The SPOT HRV (Satellite Pour l'Observation de la Terre High Resolution Visible) and Landsat ETM+ (Enhanced Thematic Mapper Plus) satellite sensors provide multi-spectral imagery in the visible and near-infrared (NIR) domains at a spatial resolution (20 m and 30 m, respectively) that is spatially consistent with the dimensions of the estuary. The aim was to obtain information at different spatial scales from the observed gradients of turbidity concerning the: long-term tidal and seasonal movements of the MTZ within the whole estuary; short-term local re-suspension phenomena over shorebanks and/or shallow waters; short-term turbulent phenomena resulting from the tidal currents and bathymetry of the estuary.

2. Theoretical background

2.1 *Satellite sensor reflectance measurements and atmospheric corrections*

The signal recorded by ocean colour satellite sensors at the top of the atmosphere (TOA) is the upwelling radiance L^* ($\mathrm{W\,m^{-2}\,sr^{-1}\,nm^{-1}}$). The TOA reflectance signal, R^* (dimensionless), is then obtained by dividing L^* by the TOA solar irradiance, E_s ($\mathrm{W\,m^{-2}\,nm^{-1}}$), and by the cosine of the solar zenith angle, θ_s, (Vermote *et al.* 1997):

$$R^* = \frac{\pi L^*}{\cos(\theta_s) E_s} \tag{1}$$

The optical parameters presented here depend on the wavelength (λ), but the symbol

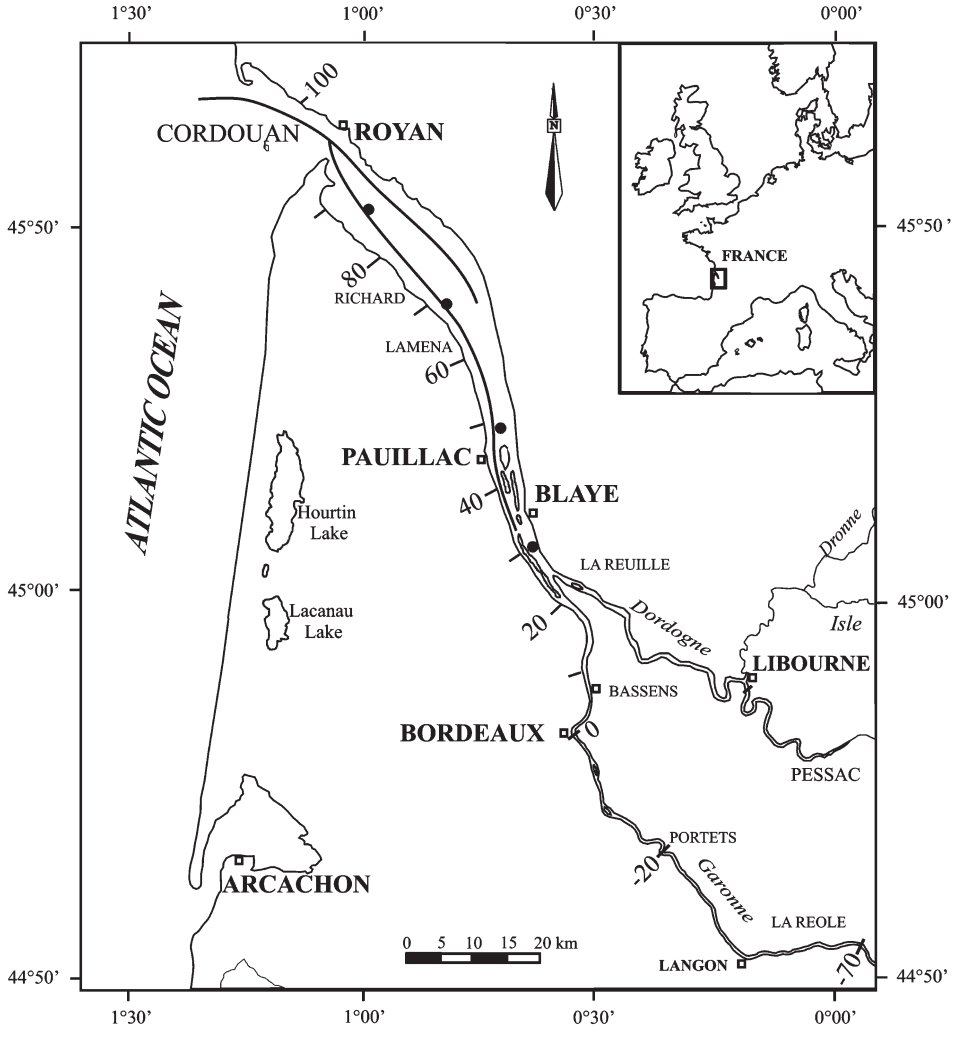

Figure 1. The Gironde estuary, located in south-west France. The lines represent the main navigation channels. Black circles locate the four stations of regular field measurements. The numbers indicate the distance (in km) from Bordeaux. These distances are called KP for kilometre points.

is omitted for clarity. R^* can be written as (modified from Gordon and Wang 1994):

$$R^* = R_{\text{ray}} + R_{\text{aer}} + R_{\text{ray/aer}} + R_{\text{gsun}} + R_{\text{gsky}} + tR_{\text{w}} \tag{2}$$

where R_{ray}, R_{aer} and $R_{\text{ray/aer}}$ are respectively the reflectance due to scattering by air molecules (Rayleigh scattering), scattering by aerosols, interaction between molecular and aerosol scattering; R_{gsun} and R_{gsky} are the reflectance of the solar beam (sun and sky glint, respectively), t is the diffuse atmospheric transmittance (dimensionless) and R_{w} is the water-leaving reflectance.

The term R_{gsun} can be ignored when the scan plane viewed by the satellite sensor is away from the specular image of the Sun. The term $R_{\text{ray/aer}}$ is zero in the single-scattering assumption, and can be ignored as long as the multiple scattering is small, i.e. at small Rayleigh and aerosol optical thickness. R_{w} is the component of interest

for bio-optical applications. The purpose of atmospheric correction is to retrieve R_w from equation (2), i.e. to correct the measured R^* signal for the Rayleigh and aerosol contributions.

The Rayleigh contribution can be estimated using a radiative transfer code that integrates predefined atmospheric models (e.g. Vermote *et al.* 1997). On the contrary, the aerosol concentration and optical properties are highly variable and cannot be predicted *a priori* (Gordon and Wang 1994, Antoine and Morel 1998). The general approach of the correction algorithm is to use spectral bands for which R_w is known to estimate the aerosol contribution. In oceanic Case 1 waters (beyond the influence of terrigeneous substances (Morel and Prieur 1977)), R_w becomes zero in the NIR and the term $(R_{aer} + R_{ray/aer})$ can be determined, then extrapolated to visible bands using the Ångström or an equivalent exponent (e.g. Gordon and Wang 1994, Antoine and Morel 1998). This method, known as the black target method (Chavez 1988), is not valid over turbid coastal (Case 2) waters where R_w is no longer zero in the NIR. In this case, a 'bright pixel' correction algorithm must be used (Moore *et al.* 1999, Lavender and Nagur 2002). However, applying such an algorithm requires the use of, at least, two NIR spectral bands and a good signal: noise ratio, which is normally only found in ocean colour sensors.

2.2 *Field reflectance measurements related to water constituents*

The second step in the satellite sensor data processing consists of obtaining information concerning the water body (nature, concentration and optical properties of the water constituents) from the retrieved R_w signal.

R_w is the ratio between the above-water upwelling radiance and the incident irradiance signal just above the water surface. Thus, for oceanographic remote sensing applications, a specific water reflectance signal called remote sensing reflectance (R_{rs}, in sr^{-1}) has been defined (Mobley 1999):

$$R_{rs}(sr^{-1}) = \frac{L_w}{E_d} \tag{3}$$

where L_w ($W\,m^{-2}\,sr^{-1}\,nm^{-1}$) is the water-leaving radiance and E_d ($W\,m^{-2}\,nm^{-1}$) is the downwelling irradiance incident above the water surface. To relate the R_{rs} and R_w signals, the reflectance bidirectional aspects must be considered (Morel and Gentili 1993, 1996).

R_{rs} is a function of the inherent optical properties (IOP), namely the absorption and backscattering coefficients (a and b_b) (Gordon *et al.* 1975, Morel and Prieur 1977), and also depends on geometrical parameters resulting from the air–water surface transfer and bidirectional aspects. In the case of the turbid waters of the Gironde estuary, Doxaran *et al.* (2002a, b) obtained:

$$R_{rs} \approx 0.524 \frac{f}{Q} \left(\frac{b_b}{a + b_b} \right) \tag{4}$$

where f (dimensionless) is a function depending on illumination conditions and water types; Q (sr) is defined as the ratio between the upwelling radiance (L_u, in $W\,m^{-2}\,sr^{-1}\,nm^{-1}$) and the upwelling irradiance signals, at null depth (i.e. just below the surface). These f and Q parameters represent the bi-directional aspects of the reflectance signal (Morel and Gentili 1993, 1996).

In coastal sediment-dominated waters, the IOP (a and b_b total coefficients) can be written as the sum of the contributions of the different water constituents classified

as pure water (w), coloured dissolved organic matter (y) and sediments (s) (Forget *et al.* 1999):

$$a = a_w + a_y + a_s \tag{5}$$

$$b_b = b_{bw} + b_{bs} \tag{6}$$

When modelling the IOP, equations (5) and (6) can be rewritten introducing the concentration of each constituent and its specific optical properties (absorption backscattering) per unit of concentration (e.g. Forget *et al.* 1999, 2001, Lahet *et al.* 2000). Such a model has been applied to the turbid sediment-dominated waters of the Gironde estuary (Doxaran *et al.* 2002a). The results obtained showed that specific R_{rs} ratios between the NIR (700–900 nm) and the visible 400–700 nm) spectral wavebands, relatively insensitive to the variations in the *SPM* characteristics (grain size, refractive index), are highly correlated with the *SPM* concentration. Thus, improved *SPM* quantification relationships may be established using R_{rs} ratios, and applied to satellite measurements corrected for atmospheric effects.

3. Data and methods

3.1 *Satellite sensor and field data*

The SPOT 1, 2, 3 HRV sensor has two wavebands in the visible portion of the electromagnetic spectrum, XS1 (500–590 nm) and XS2 (610–680 nm), and one waveband in the NIR portion of the electromagnetic spectrum, XS3 (790–890 nm) (website http://www.spotimage.fr/accueil/system/introsat/select/welcome.htm). The Landsat ETM + sensor has three bands in the visible portion of the electromagnetic spectrum, L1 (450–515 nm), L2 (525–605 nm) and L3 (630–690 nm), and two bands in the NIR portion of the electromagnetic spectrum, L4 (750–900 nm) and L5 (1550–1750 nm) (website http://landsat.gsfc.nasa.gov/guides/Landsat-7_dataset). Seven satellite sensor images of the Gironde estuary were considered in this study: six SPOT images recorded in 1996 and 2001; and one Landsat image recorded in 2000 (table 1). They correspond to different periods of the year, thus different river discharges and different tidal conditions (high/low water, spring/neap tide). The corresponding river discharge in the estuary is expressed as the sum of the respective Garonne and Dordogne river discharges (mean value during the 30 days preceding the satellite image acquisition, noted Q_{30} in $m^3 s^{-1}$) (table 1). It varies from about $350\,m^3 s^{-1}$ to $500\,m^3 s^{-1}$ during the summer period (July–August) and from

Table 1. Details of the selected satellite images of the Gironde estuary and the hydrodynamic conditions at the moment of the satellite data acquisition.

Image date	Time (GMT)	Satellite	Sensor	High tide (KP 85)	Tide	Q_{30} ($m^3 s^{-1}$)
14 July 1996	11h 23′40	SPOT-3	HRV-1	15:48	Mean	425
08 March 2000	10h 40′22	LANDSAT7	ETM +	05:42	Spring	1455
20 May 2001	11h 10′23	SPOT-2	HRV-1	14:40	Mean	1749
31 May 2001	10h 58′50	SPOT-2	HRV-2	11:58	Neap	1662
31 May 2001	11h 30′51	SPOT-1	HRV-2	11:58	Neap	1662
2 July 2001	11h 15′49	SPOT-1	HRV-1	14:23	Mean	506
17 August 2001	11h 31′53	SPOT-1	HRV-1	12:59	Mean	345

Q_{30} is the mean river inflow (Garonne + Dordogne) during the previous 30 days.

1450 $m^3 s^{-1}$ to 1750 $m^3 s^{-1}$ in March and May (peak spring floods). Most of the images correspond to neap or mean tides; only the Landsat image (8 March 2000) was recorded during a maximum spring tide. Different moments of the diurnal tide are encountered; two images were recorded the same day (31 May 2001) with a time difference of 30 minutes. This dataset is consequently representative of various seasonal and hydrodynamic conditions in the estuary.

No simultaneous *in situ* measurements were carried out concurrently with the satellite overpasses. However, numerous field data have been recorded in the Gironde estuary between 1996 and 2001. Field data include simultaneous measurements of R_{rs} and *SPM* concentrations recorded in 132 stations (18 stations in 1996, 27 in 1997; 32 in 1999; 39 in 2000 and 16 in 2001) located in different parts of the estuary (Doxaran *et al.* 2002a, b, 2003). The R_{rs} signal was determined from above-water optical measurements (380–1100 nm) carried out using a Spectron SE-590 spectroradiometer (256 channels, acceptance angle or field-of-view of 6°). Various conditions of tide and river flow were encountered during these field measurements. The corresponding *SPM* concentration range is 10–2000 $mg l^{-1}$.

3.2 *Methods*

The general method selected to quantify *SPM* concentrations in the Gironde estuary from satellite sensor (SPOT HRV, Landsat ETM+) data is presented in detail by Doxaran *et al.* (2002a). Based on field optical measurements, an invariant relationship is established between the R_{rs} signal integrated into satellite sensor spectral wavebands and the observed *SPM* concentration. The relationship obtained is then applied to satellite sensor data corrected previously for atmospheric effects, independently of their date of acquisition.

3.2.1 Quantification relationships. In the Gironde estuary, from all the field measurements carried out during the six year study (1996–2001), invariant relationships have been established using R_{rs} ratios between the NIR and the visible spectral wavebands (Doxaran *et al.* 2002a, b, 2003). Integrated into SPOT and Landsat spectral wavebands, these exponential calibration curves are written, respectively (Doxaran *et al.* 2003):

$$SPM = 27.424 \exp\left[0.0279 \frac{R_{rs}(XS3)}{R_{rs}(XS1)}\right], \quad R^2 = 0.89 \tag{7}$$

and:

$$SPM = 29.022 \exp\left[0.0335 \frac{R_{rs}(L4)}{R_{rs}(L2)}\right], \quad R^2 = 0.88 \tag{8}$$

These empirical results have thus confirmed the theoretical ones obtained using the bio-optical model, concerning the limited influence of the *SPM* characteristics (grain size, refractive index) on the selected R_{rs} ratios (Doxaran *et al.* 2002a). Relationships (7) and (8) are consequently appropriate to quantify *SPM* in the Gironde estuary from, respectively, SPOT HRV and Landsat ETM+ data recorded from 1996 to 2001. Moreover, because of the limited spectral variations of the f/Q ratio in equation (4), the use of R_{rs} ratios is expected to minimize the bi-directional effects (Morel and Gentili 1996).

Based on all the field measurements, it is possible to determine how accurately the *SPM* concentration is estimated from a R_{rs} ratio, using the established exponential

relationships (equations (7) and (8)). If SPM_{meas} and SPM_{est} are respectively the measured SPM concentration and the estimated SPM concentration given by equations (7) and (8), the difference is:

$$diff_{SPM} = \frac{SPM_{est} - SPM_{meas}}{SPM_{meas}} \quad (9)$$

The mean value of $diff_{SPM}$ is $\pm 25\%$ (SD=21%) for relationship (7), corresponding to SPOT bands, and $\pm 25\%$ (SD=23%) for relationship (8), corresponding to Landsat bands. The observed differences essentially depend on the errors occurring during the *in situ* measurements, due notably to changing surface reflection effects, water turbidity and incident light variations. The percentage error on the retrieved SPM concentrations can be minimized by considering only data collected during optimum environmental conditions (e.g. plane sea surface, clear sky) (Doxaran *et al.* 2002b).

3.2.2 Atmospheric corrections. Before applying the established quantification relationships, the selected satellite sensor data recorded in the NIR and visible portions of the electromagnetic spectrum were corrected for atmospheric effects. Because of the limited number of spectral wavebands in the NIR portion of the electromagnetic spectrum and the relative insensitivity of the sensors, recently developed correction algorithms cannot be applied to the selected SPOT HRV and Landsat ETM+ data. The correction method selected in this study is consequently similar to the one presented by Doxaran *et al.* (2002a). The reflectance of the direct solar beam, R_{gsun} in equation (2), was assumed to be zero. The term $R_{ray/aer}$ was also assumed to be insignificant (single-scattering assumption). The atmospheric gaseous composition (R_{ray}) was defined by selecting an appropriate atmospheric model in the 6s radiative transfer code (Vermote *et al.* 1997) (table 2). R_{gsky} is computed exactly in the 6s code with the Snell–Fresnel laws. Then, the black target method (Chavez 1988) was used to estimate the aerosol contribution in the NIR. The black targets were located where the R^* signal was minimum in the NIR and the

Table 2. Satellite atmospheric correction parameters – the selected 6s atmospheric and aerosol models, the black target on the image and the corresponding vertical visibility.

Date	6s atm. model	Black target	6s aerosol model	Visibility (km)
14 July 1996	Mid-latitude Summer	Hourtin Lake	39% DL, 15% WS, 40% O, 1% S	13
8 March 2000	Mid-latitude Winter	Lacanau Lake	95% O, 5% WS	15
20 May 2001	Mid-latitude Summer	Hourtin Lake	50% DL, 50% O	20
31 May 2001 (a)	Mid-latitude Summer	Continental shelf waters	39% DL, 15% WS, 40% O, 1% S	9
31 May 2001 (b)	Mid-latitude Summer	Lacanau Lake	4% DL, 6% WS, 90% O	12
2 July 2001	Mid-latitude Summer	Continental shelf waters	70% DL, 29% WS, 1% S	10
17 August 2001	Mid-latitude Summer	—	70% DL, 29% WS, 1% S	15

Note: DL, dust-like; WS, water soluble; O, oceanic and S, soot.

corresponding recorded R^* signal was assumed to be purely atmospheric ($R_w=0$). Depending on the satellite sensor image, the identified black targets correspond to lake waters (Hourtin and Lacanau, south of the estuary (figure 1)) and/or continental shelf waters beyond the influence of the turbid plume (table 2). The aerosol contribution in the NIR wavebands (λ_{NIR}) was then deduced from equation (2):

$$R_{aer}(\lambda_{NIR}) = R^*(\lambda_{NIR}) - R_{ray}(\lambda_{NIR}) \tag{10}$$

Considering the two NIR wavebands, noted λ_{NIR1} and λ_{NIR2}, the Ångström coefficient (n), was determined as (e.g. Moore *et al.* 1999):

$$n = -\ln\left[\frac{R_{aer}(\lambda_{NIR1})}{R_{aer}(\lambda_{NIR}2)}\right] \Big/ \ln\left(\frac{\lambda_{NIR1}}{\lambda_{NIR2}}\right) \tag{11}$$

n was used to determine the aerosol contribution in the remaining visible wavebands (λ_{VIS}) (Vermote *et al.* 1997):

$$R_{aer}(\lambda_{vis}) = R_{aer}(\lambda_{NIR2})\left(\frac{\lambda_{VIS}}{\lambda_{NIR2}}\right)^{-n} \tag{12}$$

The L4 and L5 wavebands of the Landsat ETM + sensor were selected as λ_{NIR1} and λ_{NIR2}, respectively, for these computations. The SPOT HRV sensor has only one NIR waveband (XS3=λ_{NIR2}). It was consequently assumed that the water-leaving radiance in the red waveband (XS2) was also zero over black targets, and the waveband XS2 was used as λ_{NIR1} in equation (11). Such an assumption may have led to a slight overestimation of the aerosol contribution because the contribution from the water may not be negligible in this case.

The 6s aerosol model, initially approximately selected according to available meteorological data (wind speed and direction, horizontal visibility, pressure, humidity provided by METEO-FRANCE in four stations surrounding the estuary), was fitted in order to retrieve the calculated R_{aer}. The advantage of this method was to take into account both available meteorological data and radiometric measurements recorded by the satellite sensors. The resulting aerosol models and vertical visibility reproduced by 6s are presented in table 2.

Once the atmospheric and aerosol models were defined in 6s, the different terms in equation (2) (reflectance, transmittance), in the visible and NIR spectral wavebands, were identified. The atmosphere was assumed to be homogeneous over the whole satellite image. In order to validate the corrections, the R_w values retrieved over the estuarine waters and the Médoc sand beaches were finally compared to typical field reflectance measurements.

In clear oceanic waters, the water-leaving reflectance generally represents about 10% of the TOA signal (Mobley 1994). Based on our corrections, quite different results were obtained in the case of the highly turbid waters of the Gironde estuary. Over the estuary, the water-leaving reflectance contribution to the TOA reflectance, expressed as the ratio (R_w/R^*), was observed to be higher than 60%. It was slightly lower in the NIR than in the visible, but increased to 90% in the parts of the estuary where the retrieved R_w was maximum (i.e. where *SPM* concentrations were maximum). Thus, the influence of the atmosphere over such highly turbid waters appeared to be limited. Without field reflectance measurements concurrently with the satellite overpass, it is difficult to estimate the uncertainty of the applied

atmospheric correction. However, this uncertainty only concerned a low percentage (typically 20%) of the TOA signal over the estuary.

As a practical consequence, the uncertainty in the *SPM* concentrations retrieved from satellite data depended essentially on the established quantification relationships (equations (7) and (8)). A global uncertainty around $\pm 40\%$ can reasonably be expected.

4. Results

Quantification relationships were finally applied to the atmospherically corrected SPOT HRV and Landsat ETM+ data. As a result, for each image, a horizontal *SPM* distribution was established within the surface waters of the estuary where suspended sediment and phytoplankton (chlorophyll-*a*) concentrations typically vary in the range 10–2000 $mg\,l^{-1}$ and 1–3 $\mu g\,l^{-1}$, respectively (Irigoien and Castel 1997, Abril *et al.* 1999). *SPM* values estimated from remote sensing data can therefore be related to suspended sediment concentrations, in a first approximation. The obtained results are first analysed at a large scale in order to locate and observe the tidal/seasonal movements of the MTZ. Then, results are analysed in term of detailed turbidity features observed from satellite measurements and related to hydrodynamic calculations.

4.1 *Location and movements of the MTZ*

The first image (SPOT HRV, 14 July 1996, 11h 23) presents the situation during a low river flow and mean tide conditions (figure 2(*a*)). It was recorded during the start of the flood in the downstream part of the estuary, corresponding to slack low water in the central part and the ending ebb in the upstream part (low water + 01h 30 at KP 85). Decreasing *SPM* concentrations from 1000 $mg\,l^{-1}$ to less than 50 $mg\,l^{-1}$ are observed from the upstream part to the mouth. A first and main MTZ is located upstream of the confluence zone of the rivers (KP 25). A second MTZ is observed in the upstream/central part of the estuary, around the islands. High *SPM* concentrations are retrieved all along the main navigation channel (left shore) between KP 25 and 65. Suspended sediments transported downstream during the ending ebb tide draw turbulent features in this channel.

The second image (Landsat ETM+, 8 March 2000, 10h 40) is representative of very different conditions: maximum spring tide and high river flow (peak flood). It was taken around mid ebb in the central part of the estuary (low water – 01h 30 at KP 85). High *SPM* concentrations are observed in the whole estuary (figure 2(*b*)). The lowest *SPM* concentrations are located in the rivers and in the upstream part. In the central and downstream parts, the turbidity is very heterogeneous. *SPM* concentrations are also high near the mouth where suspended sediments are transported by ebb currents towards the ocean, notably along the main channel. Consequently the MTZ is stretched out over the central and downstream parts of the estuary, and partly expelled towards the ocean during the ebb.

The third image (SPOT HRV, 20 May 2001, 11h 10) was recorded on the last day of a six-month-long high river flow period, at mean tide. It was around mid-ebb (low water + 03h 00 at KP 85). *SPM* concentrations are low in the rivers and the upstream and downstream parts of the estuary (typically 50–100 $mg\,l^{-1}$). Turbid waters with *SPM* of 200–300 $mg\,l^{-1}$ are retrieved in a confined area located in the central part, between KP 65 and 75 (figure 3(*a*)). High *SPM* concentrations are also

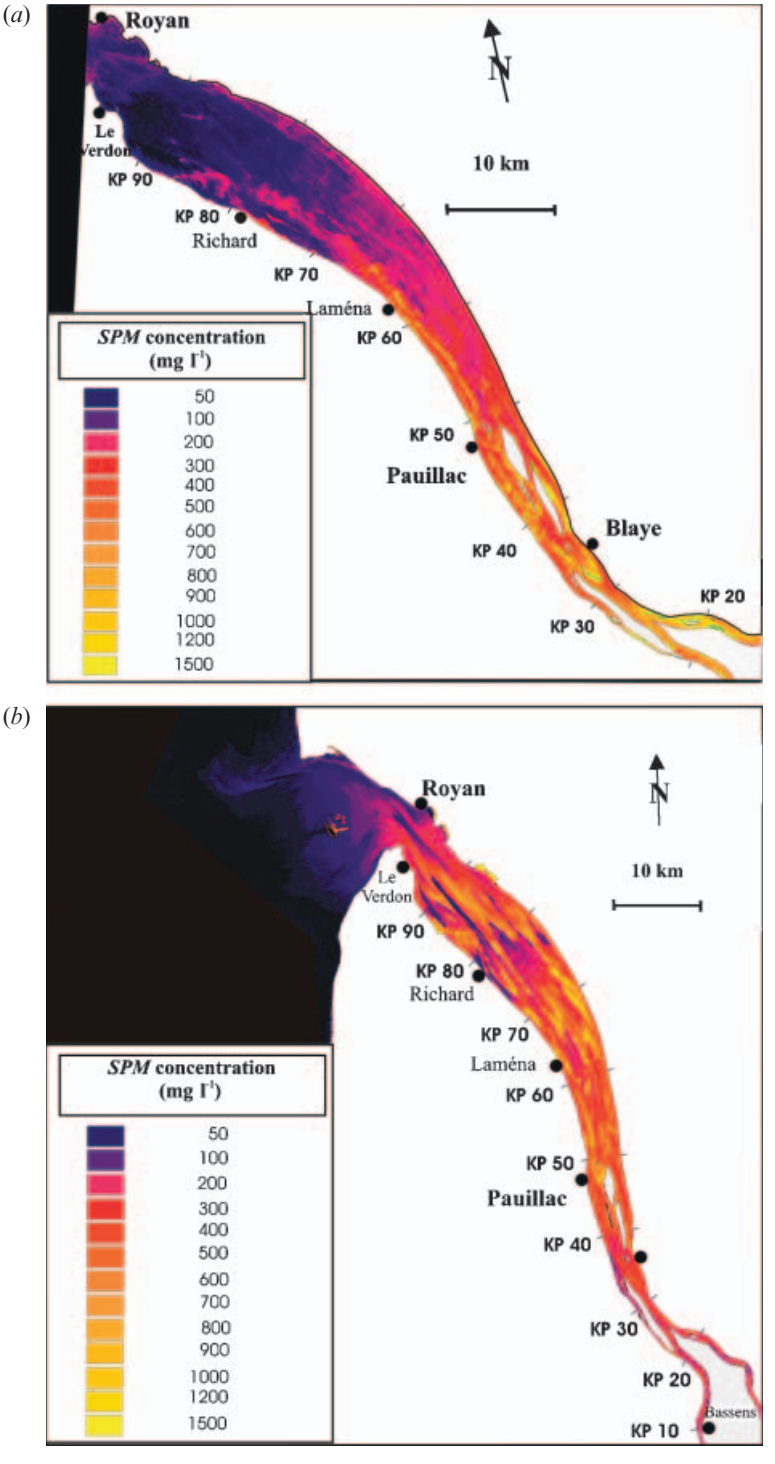

Figure 2. Horizontal *SPM* distributions in the Gironde estuary retrieved from (*a*) SPOT data recorded the 14 July 1996, 11h 23; (*b*) Landsat data recorded the 8 March 2000, 10h 40.

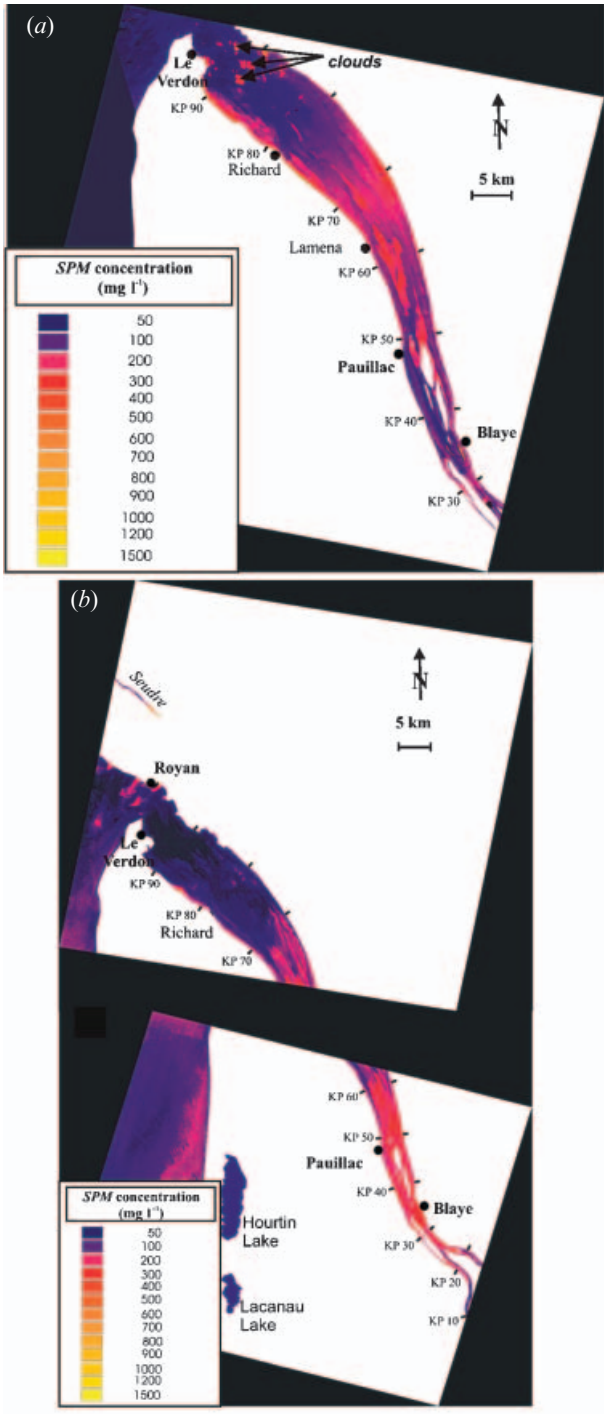

Figure 3. Horizontal *SPM* distributions in the Gironde estuary retrieved from (*a*) SPOT data recorded the 20 May 2001, 11h 10; (*b*) SPOT data recorded the 31 May 2001, 10h 58 (top) and 11h 30 (bottom).

observed in front of the KP 60, on the border of the main channel, certainly resulting from re-suspension over muddy banks. The observed situation globally corresponds to a 'residual' MTZ located in the central part of the estuary, after being largely expelled in the ocean during the high river flow period.

The river flow rapidly decreased from 20 May 2001 ($1500\,m^3\,s^{-1}$) to 31 May 2001 ($900\,m^3\,s^{-1}$). Two satellite sensor images (SPOT HRV, 31 May 2001, 10h 58 and 11h 30, respectively) show the influence of this changing river flow on the MTZ location. As a result of the decreasing river flow, the MTZ moved rapidly upstream (estimated mean velocity of 1.4 km/day), reaching the confluence zone of the Garonne and Dordogne rivers (figure 3(*b*)). High *SPM* were still observed within shallow regions around KP 60.

The next image (SPOT HRV, 2 July 2001, 11h 16) concerns only the central and downstream parts of the estuary. It was taken at mean tide, at the beginning of the low river flow period. It was mid-flood at KP 85. The MTZ is located in the central and upstream parts (figure 4(*a*)). High *SPM* are still observed over mud banks, in front of KP 60. Downstream, *SPM* are low but turbid features resulting from re-suspension phenomena can be observed, drawing the morphology of most of the mud and sandbanks.

The last image (SPOT HRV, 17 August 2001, 11h 32) concerns the central and upstream parts of the estuary. It was recorded at mean tide, after a three-month-long low river flow period. The highest *SPM* concentrations ($400–1000\,mg\,l^{-1}$) are retrieved in the rivers, up to 30 km upstream from the confluence zone (figure 4(*b*)). Surface waters are also turbid (mean *SPM* of $300\,mg\,l^{-1}$) in the upstream part, notably around the islands. In front of the KP 60, turbid features are still observed over mud banks. Thus, the satellite data locate the main MTZ into the rivers, and a secondary one in the central part of the estuary, where sediments were trapped in the island zone. This finally results in a global 70 km-long MTZ.

Because of the atmospheric correction uncertainties, the quantitative accuracy of the retrieved *SPM* concentrations was invalidated. However, the observed gradients of turbidity were assumed to be realistic because the atmospheric contribution is relatively small in turbid waters and so errors within the processing were essentially dependent on the calibration relationships between the R_{rs} signal and *SPM*. Consequently, the information extracted from the satellite data can be used to locate the MTZ and observe its tidal and seasonal movements. Therefore, in figures 2–4, the MTZ is located upstream, partly in the rivers and partly around the islands during a low river flow period. When this period is long, the sediments move inside the rivers, up to 40 km upstream from the confluence zone. However, the MTZ moves downstream from the islands and extends up to the mouth during a long high river flow period. Then, peak flood and spring tides help to partly eject the MTZ into the ocean. When the river flow decreases, the MTZ moves rapidly to the upstream part, around the islands and up to the confluence zone. When the low river flow is established, a main MTZ moves inside the rivers but a secondary MTZ remains around the islands and over local mud banks. These observations are in close agreement with knowledge concerning MTZ dynamics (e.g. Allen *et al.* 1977, Castaing 1981, Sottolichio *et al.* 2001).

During one year, from September 2000 to September 2001, vertical turbidity profile measurements were carried out monthly at four fixed stations in the estuary (figure 1). These measurements gave regular information concerning the approximate location of the MTZ and the range of surface *SPM* concentrations, which

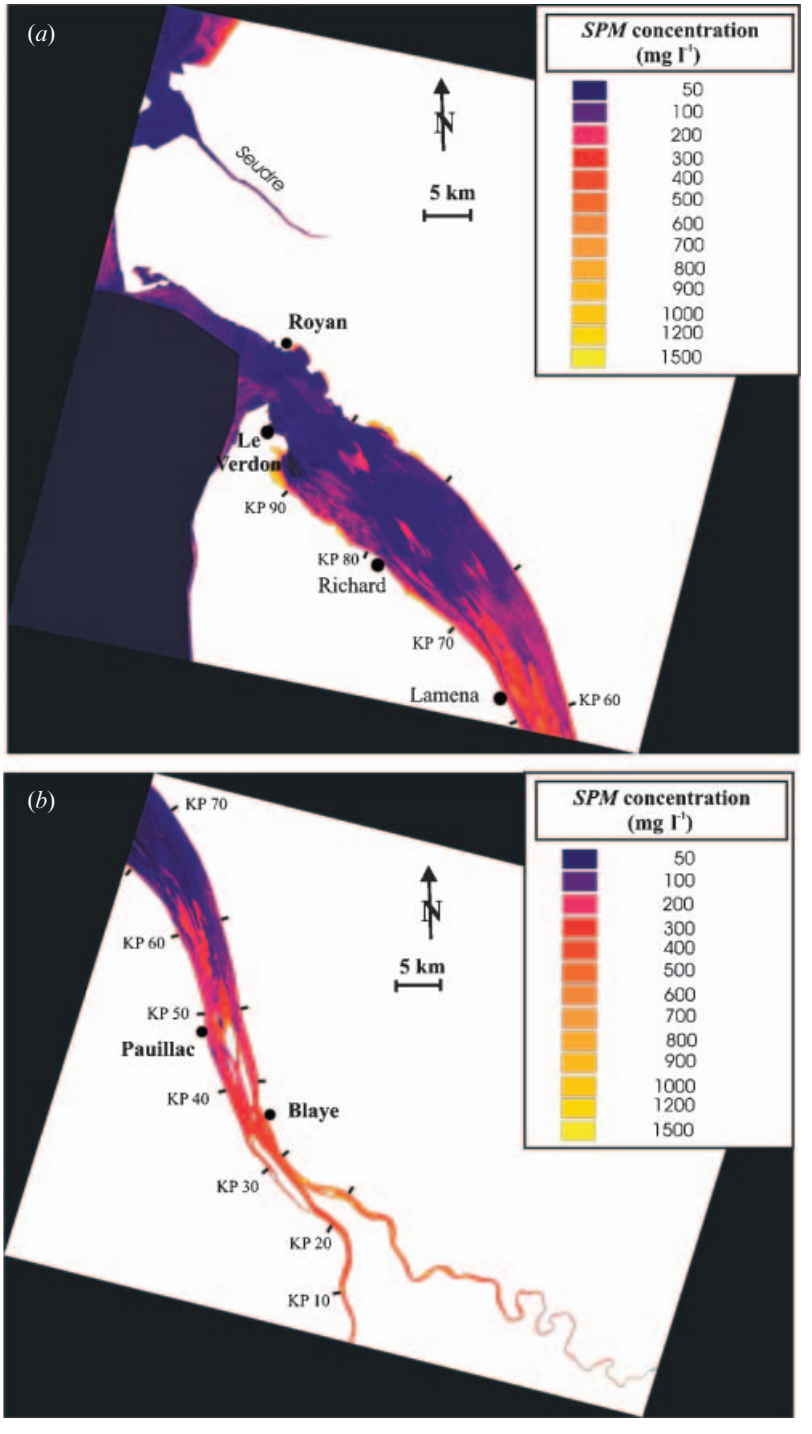

Figure 4. Horizontal *SPM* distributions in the Gironde estuary retrieved from (*a*) SPOT data recorded the 2 July 2001, 11h 16; (*b*) SPOT data recorded the 17 August 2001, 11h 32.

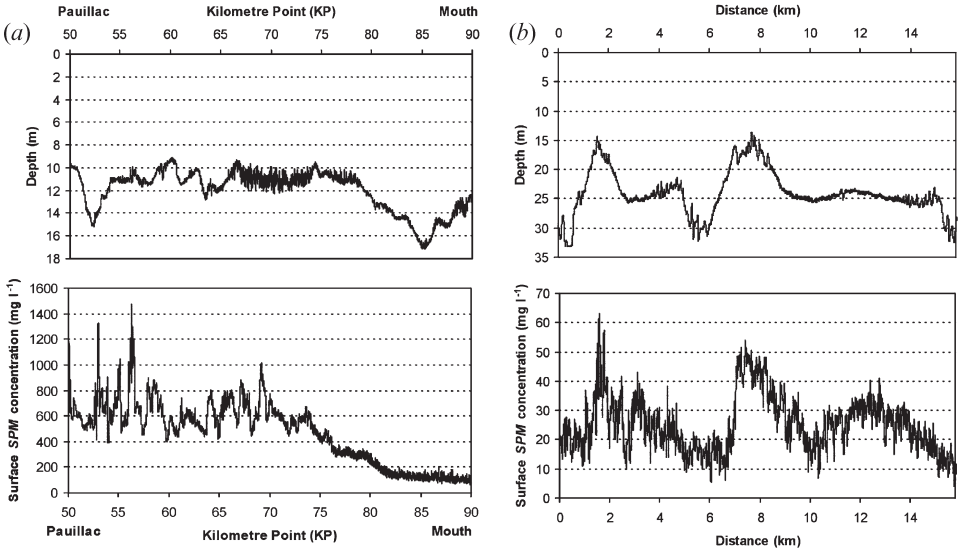

Figure 5. Water depth (top) and surface *SPM* concentration (bottom) measurements carried out along transects in the Gironde estuary, during the Girox-1 field campaign, the 19 February 2002 (mean tide): (*a*) along the navigation channel, from the mouth (KP 90) to Pauillac (KP 48) (transect started at 16h 00); (*b*) in the mouth area (KP 87–90) (transect started at 05h 30, mid-flood).

appeared to be in good agreement with satellite observations (Doxaran 2002). The purpose of this research was not to compare satellite-derived turbidity with field observations. However, it is interesting to present some field measurements showing the typical range of *SPM* concentrations within surface waters of the Gironde estuary and highlight the influence of the bathymetry. The 19 February 2002 (Girox-1 field campaign), water depths and surface *SPM* concentrations were measured along transects covering the mouth area (KP 87–90), then along the navigation channel from the mouth (KP 90) to Pauillac (KP 50). Turbidity measurements were recorded by an Optical Backscattering Sensor (OBS) sensor fixed 50 cm below the water surface. Water samples were collected regularly to determine surface *SPM* concentrations and establish a calibration curve for the turbidity sensor (Doxaran 2002). During the two-hour transect along the navigation channel, *SPM* concentrations increased from about $100\,mg\,l^{-1}$ near the mouth to $700\,mg\,l^{-1}$ near Pauillac (figure 5(*a*)). Concentration peaks higher than $1000\,mg\,l^{-1}$ (KP 53–58) and around $800\,mg\,l^{-1}$ (KP 65–70) were observed frequently, but the influence of bathymetry was almost insignificant. This indicated that turbidity within surface waters mainly resulted from the MTZ location. On the contrary, a strong bathymetric influence was observed near the mouth, during a one-hour transect corresponding with the mid-flood tide. Surface *SPM* concentrations, ranging from 10 to $60\,mg\,l^{-1}$, typically increased with decreasing water depth, clearly showing the predominant influence of lower water depths (figure 5(*b*)). These typical field observations are in close agreement with satellite observations in terms of surface *SPM* concentration range, MTZ location and the influence of bathymetry in the downstream part of the estuary.

4.2 *Detailed turbidity features*

Using the high spatial resolution of SPOT HRV and Landsat ETM + data, it is also possible to observe fine-scale turbidity features in the estuary, such as re-suspension phenomena (Doxaran *et al.* 2002a). In this case, suspended particles are used as current markers and the observed gradients of turbidity provide information concerning instantaneous flows within the surface waters.

The example presented here (figure 6(*a*)) shows turbulent flows located in the upstream part of the Gironde estuary, observed on the SPOT HRV image acquired on 14 July 1996. A first interesting pattern (1) is observed at the confluence area of the Garonne and Dordogne rivers (KP 28 to KP 30). Turbulent flows, identified with increasing gradients of turbidity from the shore to the middle of the channel, are developed along about two kilometres. A second interesting pattern (2) is located between KP 30 and KP 45, along the main navigation channel. In this area, the channel is about 800 m wide and around 12 m deep. A type of turbulent 'helicoidal' is observed in this area. It is developed along 10 km, with an approximate wavelength of 1.6 km and mean amplitude of 0.7 km.

In order to interpret the observed phenomena, appropriate hydrodynamic information is necessary. At the moment of the satellite sensor data acquisition, instantaneous current velocities in the estuary have been calculated with the SAM-2D two-dimensional hydrodynamic model (Sottolichio *et al.* 2001). Superimposing the computed depth-averaged velocities onto the satellite sensor image allows the interpretation of the observed phenomena (figure 6(*b*)). The turbulent flows in the confluence zone result from the mixing of waters supplied by the Garonne and Dordogne rivers during the ebb. The mixed waters are then divided in front of KP 30 (Plassac bank) and separate flows are established on the two sides of the islands. Along the left shore, ebb current velocities are maximum in the middle of the narrow navigation channel (6–8 m depth and 170–300 m wide) and slightly lower on its

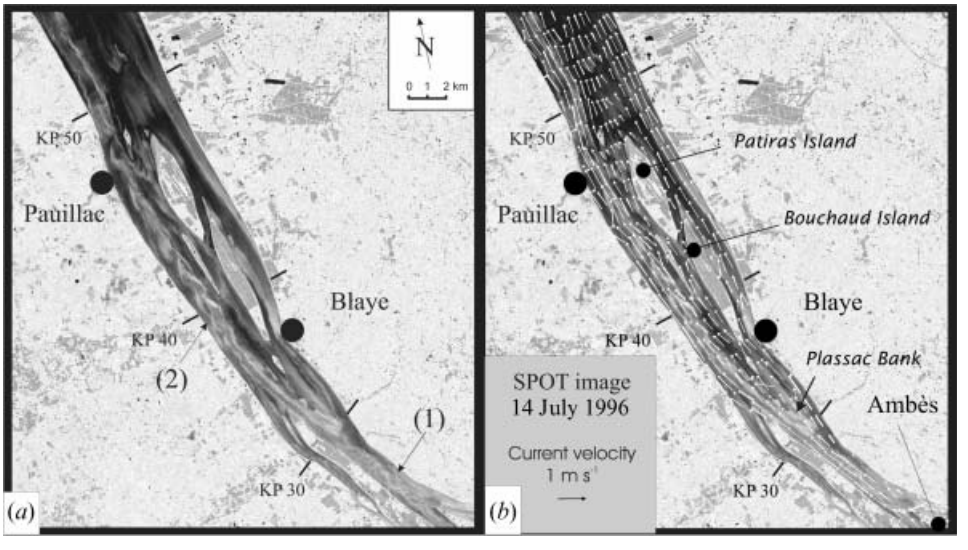

Figure 6. Example of detailed turbidity features observed on the SPOT image recorded on 14 July 1996. (*a*) Turbulent currents can be observed in the upstream part of the Gironde estuary. (*b*) Superposition of instantaneous current velocities calculated with the SAM-2D hydrodynamic model at the moment of satellite data acquisition.

border (where water depths are typically lower than 5 m). The model does not reproduce the observed 'helicoidal' current. This turbulence may only concern the surface waters viewed by the satellite sensor (due to high *SPM* concentrations, the water depth viewed by the satellite is expected to be less than 1 m (Irigoien and Castel 1997)). This would explain why the turbulence is not reproduced by the depth-averaged calculations of the model. Another possible explanation is that the turbulence results from fine-scale induced phenomena notably related to the morphology of the channel (which is narrow and presents strong depth variations between the left shore and the islands). The large computational grid of the model ($200 \times 500\,m^2$ in this area) may not be adapted to reproduce such detailed turbulent features. In both cases, the use of a three-dimensional model with a refined computational grid is necessary for clarification.

5. Conclusions

A simple and operational method was applied to quantify *SPM* concentrations in the turbid Gironde estuarine waters using SPOT HRV and Landsat ETM+ imagery. The method is based on a calibrated relationship between R_{rs} ratios (NIR/VIS) and *SPM* which is valid for long-term use. Before applying this relationship, satellite data were corrected for atmospheric affects, using a radiative transfer code, assuming that the atmosphere was homogeneous over the whole image. This simple correction scheme may be enhanced, notably using recently revealed 'pixel by pixel' corrections schemes (e.g. Moore *et al.* 1999) and considering multi-spectral sensors (i.e. several narrow wavebands in the NIR spectral domain (700–900 nm), used to determine the aerosol contribution). A study is also necessary to quantitatively assess the influence of the atmospheric correction uncertainty on the retrieved *SPM*. However, based on the applied correction, it was interesting to observe the reduced influence of the atmosphere on satellite sensor data over highly scattering estuarine waters. As a consequence, the *SPM* retrieval uncertainty essentially depends on the calibration relationships between the R_{rs} signal and *SPM*.

Applied to a set of selected SPOT HRV and Landsat ETM+ images, the obtained results have highlighted the considerable potential of remote sensing measurements in turbid estuarine waters. Each image enables the MTZ to be located with an accuracy that cannot be obtained from field measurements or sediment transport models. The observations, in close agreement with current knowledge concerning seasonal movements of the MTZ (Castaing 1981, Sottolichio *et al.* 2001), have notably revealed the existence of two regular MTZ and specific areas predominantly influenced by re-suspension phenomena in the Gironde estuary. This knowledge has been oversimplified because of the lack of regular large-scale field observations (costly in terms of time and material), but satellite remote sensing addresses this lack of information and provides measurements with a high spatial resolution.

As a first conclusion, SPOT HRV and Landsat-ETM+ satellite data can be used to map the water surface turbidity over the whole estuary with a high spatial resolution (around 30 m). They provide information at different spatial and temporal scales in terms of sediment transport and hydrodynamics. Images recorded on a monthly basis can be used to locate the MTZ and thus observe the large-scale *SPM* seasonal movements.

In the future, the use of SPOT HRV and Landsat-ETM+ can be combined with additional satellite sensors (also with a spatial resolution of ca 25 m), such as the Compact High Resolution Imaging Spectrometer – Project for On Board Autonomy

(CHRIS-PROBA), ASTER and Hyperion. This would provide enhanced overpass opportunities and could therefore create an operational system to provide regular observations of *SPM* seasonal movements. To complement these long-term observations, information concerning the tidal *SPM* dynamics may be obtained from airborne sensor data (e.g. using the Compact Airborne Spectrographic Imager, CASI). Airborne systems have the added advantage of being flexible and so can be flown at times specified by the user and hence several times within a tidal cycle, but cover a much smaller spatial extent and so several flightlines would need to be mosaicked together to cover the whole estuary.

Moreover, the spatial resolution of SPOT HRV and Landsat-ETM+ satellite sensors has provided detailed information on fine-scale turbidity features, such as re-suspension phenomena along shore-banks and high-bottoms, turbulent flows developed in the main navigation channel. As these phenomena have a short life period (from one minute to one hour) and develop over areas of several hundred metres, they have rarely been observed from field measurements. Remote sensing measurements with a very high spatial resolution could therefore provide an ideal method of observation. Satellite (e.g. SPOT-5, IKONOS) and airborne sensors (e.g. CASI), with associated spatial resolutions ranging from 3–10 m, represent a new source of information in this domain.

In both cases, an understanding of the observed phenomena and associated processes involves the use of three-dimensional hydrodynamic and sediment transport models. In order to reproduce the actual sediment dynamics, such models will have to cover the whole estuary without neglecting fine-scale induced phenomena occurring in critical areas (shore-banks, shallow-water depths and main channels). The future challenge will aim to integrate the information extracted from remote sensing data into such models (e.g. Vos *et al.* 2000) in order, notably, to quantify sedimentary fluxes.

Acknowledgement

This research was supported through a Région Aquitaine fellowship, then through a European Community Marie Curie fellowship (NCR 70037, Fifth Framework Programme). The authors express particular thanks to Dr J. M. Froidefond, Mr G. Oggian and Mr H. Derriennic (Université Bordeaux 1) for their contribution.

References

Abril, G., Etcheber, H., Le Hir, P., Bassoullet, P., Boutier, B. and Frankignoulle, M., 1999, Oxic/anoxic oscillations and organic carbon mineralization in an estuarine maximum turbidity zone (The Gironde, France). *Limnology and Oceanography*, **44**, pp. 1304–1315.

Allen, G.P., Sauzay, G., Castaing, P. and Jouanneau, J.M., 1977, Transport and deposition of suspended sediment in the Gironde estuary, France. In *Estuarine Processes*, M. Wilet (Ed.), pp. 63–81 (New York: Academic Press).

Antoine, D. and Morel, A., 1998, Relative importance of multiple scattering by air molecules and aerosols in forming the atmospheric path radiance in the visible and near-infrared parts of the spectrum. *Applied Optics*, **37**, pp. 2245–2259.

Cancino, L. and Neves, R., 1999, Hydrodynamic and sediment suspension modelling in estuarine systems; Part II: Application to the Western Scheldt and Gironde estuaries. *Journal of Marine Systems*, **22**, pp. 117–131.

Castaing, P., 1981, Le transfert à l'océan des suspensions estuariennes. Cas de la Gironde. Thèse d'Etat, Université Bordeaux 1 (France), n° 701.

Chavez, P.S., Jr, 1988, An improved dark-object substraction technique for atmospheric scattering correction of multispectral data. *Remote Sensing of Environment*, **24**, pp. 459–479.

Douillet, P., Ouillon, S. and Cordier, E., 2001, A numerical model for fine suspended sediment transport in the south-west lagoon of New-Caledonia. *Coral Reefs*, **20**, pp. 361–372.

Doxaran, D., 2002, Télédétection and modélisation des flux sédimentaires dans l'estuaire de la Gironde. PhD thesis, Université Bordeaux 1, France.

Doxaran, D., Froidefond, J.M., Lavender, S.J. and Castaing, P., 2002a, Spectral signature of highly turbid waters. Application with SPOT data to quantify suspended particulate matter concentrations. *Remote Sensing of Environment*, **81**, pp. 149–161.

Doxaran, D., Froidefond, J.M. and Castaing, P., 2002b, A reflectance band ratio used to estimate suspended matter concentrations in sediment-dominated coastal waters. *International Journal of Remote Sensing*, **23**, pp. 5079–5085.

Doxaran, D., Froidefond, J.M. and Castaing, P., 2003, Remote sensing reflectance of turbid sediment-dominated waters. Reduction of sediment type variations and changing illumination conditions effects using reflectance ratios. *Applied Optics*, **42**, pp. 2623–2634.

Forget, P., Broche, P. and Naudin, J.J., 2001, Reflectance sensitivity to solid suspended sediment stratification in coastal water and inversion; A case study. *Remote Sensing of Environment*, **77**, pp. 92–103.

Forget, P., Ouillon, S., Lahet, F. and Broche, P., 1999, Inversion of reflectance spectra of non-chlorophyllous turbid coastal waters. *Remote Sensing of Environment*, **68**, pp. 264–272.

Gordon, H.R., Brown, O.B. and Jacobs, M.M., 1975, Computed relation between the inherent and apparent optical properties of a flat homogeneous ocean. *Applied Optics*, **14**, pp. 417–427.

Gordon, H.R. and Wang, M., 1994, Retrieval of water-leaving radiance and aerosol optical thickness over the oceans with SeaWIFS: preliminary algorithm. *Applied Optics*, **33**, pp. 443–452.

Irigoien, X. and Castel, J., 1997, Light limitation and distribution of chlorophyll pigments in a highly turbid estuary: The Gironde (SW France). *Estuarine Coastal and Shelf Science*, **44**, pp. 507–517.

Lahet, F., Ouillon, S. and Forget, P., 2000, A three component model of ocean colour and its application in the Ebro river mouth area. *Remote Sensing of Environment*, **72**, pp. 181–190.

Lavender, S.J. and Nagur, C.R.C., 2002, Mapping coastal waters with high resolution imagery: atmospheric correction of multi-height airborne imagery. *Journal of Optics*, **A4**, pp. S50–S55.

Le Hir, P., Bassoulet, P. and Jestin, H., 2001, Application of continuous modeling concept to simulate high concentration suspended sediment in a macrotidal estuary. In *Coastal and Estuarine Sediment Processes*, W.H. McAnally and A.J. Metha (Eds), pp. 229–247 (Amsterdam: Elsevier).

Mobley, C.D., 1994, *Light and water* (San Diego: Academic Press).

Mobley, C.D., 1999, Estimation of the remote-sensing reflectance from above-surface measurements. *Applied Optics*, **38**, pp. 7442–7455.

Moore, G.F., Aiken, J. and Lavender, S.J., 1999, The atmospheric correction of water colour and the quantitative retrieval of suspended particulate matter in Case II waters: application to MERIS. *International Journal of Remote Sensing*, **20**, pp. 1713–1733.

Morel, A. and Gentili, B., 1993, Diffuse reflectance of oceanic waters. II. Bidirectional aspects. *Applied Optics*, **32**, pp. 6864–6879.

Morel, A. and Gentili, B., 1996, Diffuse reflectance of oceanic waters. III. Implication of bidirectionality for the remote-sensing problem. *Applied Optics*, **35**, pp. 4850–4861.

MOREL, A. and PRIEUR, L., 1977, Analysis of variations in ocean color. *Limnology and Oceanography*, **22**, pp. 709–722.

SIEGEL, H., GERTH, M. and MUTZKE, A., 1999, Dynamics of the Oder river plume in the Southern Baltic Sea: satellite data and numerical modelling. *Continental Shelf Research*, **19**, pp. 1143–1159.

SOTTOLICHIO, A., LE HIR, P. and CASTAING, P., 2001, Modelling mechanisms for the turbidity maximum stability in the Gironde estuary, France. In *Coastal and Estuarine Sediment Processes*, W.H. McAnally and A.J. Metha (Eds), pp. 373–385 (Amsterdam: Elsevier).

VERMOTE, E.F., TANRE, D., DEUZE, J.L., HERMAN, M. and MORCRETTE, J.J., 1997, Second Simulation of the Satellite Signal in the Solar Spectrum: An Overview. *IEEE Transactions in Geosciences and Remote Sensing*, **35**, pp. 675–686.

VOS, R.J., BRUMMELHUIS, P.J.G. and GERRITSEN, H., 2000, Integrated data-modelling approach for suspended sediment transport in a regional scale. *Coastal Engineering*, **41**, pp. 177–200.